



IMR KINKEN Research Highlights 2013

著者	東北大学金属材料研究所
journal or publication title	IMR KINKEN Research Highlights
year	2013
URL	http://hdl.handle.net/10097/57368

Mechanical Properties of Ferrite-martensite Dual Phase Steels with Interphase Precipitation

Ferrite-martensite dual phase steels with interphase precipitation of nano-sized vanadium carbides were prepared and mechanical properties were systematically investigated. It was found that nano-sized vanadium carbides are effective for improving the post-uniform elongation as well as increasing the strength of dual phase steels.

Introduction

It is well known that ferrite-martensite dual phase (DP) steels exhibit high strength and good formability and has widely been in practical use [1]. Stress-strain curves of ferrite-martensite DP steels are characterized by large work-hardening and uniform elongation but small post-uniform elongation. On the other hand, interphase precipitated steels, composed of single phase ferrite and dispersion of nano-sized alloy carbides in ferrite, are also known as commercial steels having a good balance of high strength and formability [2]. Stress-strain curves of interphase precipitated steels are such that work hardening and uniform elongation are relatively low but post-uniform elongation is quite large [3]. That is, ferrite-martensite DP steels and interphase precipitated steels have both good and bad points. It may be possible to significantly improve the strength and ductility if nano-sized alloy carbides are dispersed in ferrite phase of ferrite-martensite DP steels, combining advantages of both steels, which is a motivation for the present study.

In this study, ferrite-martensite DP samples with dispersion of nano-sized vanadium carbides (VC) in ferrite phase were produced using ferrite transformation accompanied with interphase precipitation followed by water quenching in a V-added low carbon steel, and the mechanical properties of such DP samples were systematically investigated to understand the effect of nano-sized precipitates on the strength and ductility of DP steels.

Experimental

A low carbon steel with a chemical composition of Fe-0.095%C-1.49%Mn-0.43%V (in mass%) (V-added steel) was used in the present study. After austenitizing at 1100°C for 600 s, samples were isothermally transformed at 690°C for different holding periods followed by quenching, leading to ferrite-martensite DP samples accompanied with interphase precipitation of VC in ferrite. Conventional ferrite-martensite DP samples with no VC particles were also prepared using Fe-0.098%-1.5%Mn (V-free steel) for comparison. Microstructures were characterized by optical microscopy, transmission electron microscopy (TEM) and electron backscatter diffraction (EBSD). Tensile tests were carried out at room temperature at an initial strain rate of $8.3 \times 10^{-4} \text{ s}^{-1}$.

Results and Discussion

By using isothermal ferrite transformation followed by water quenching, ferrite-martensite DP samples with different volume fraction of ferrite has successfully been obtained for both V-added and V-free steels. TEM observation has confirmed that VC precipitates with an average diameter of approximately 10 nm were distributed in ferrite phase of V-added DP samples. Tensile tests were carried out for the obtained DP samples, and strength and elongation were determined from stress-strain curves. Fig. 1 shows the strength and ductility of the samples as a function of volume fraction of ferrite. It is seen that the strength of

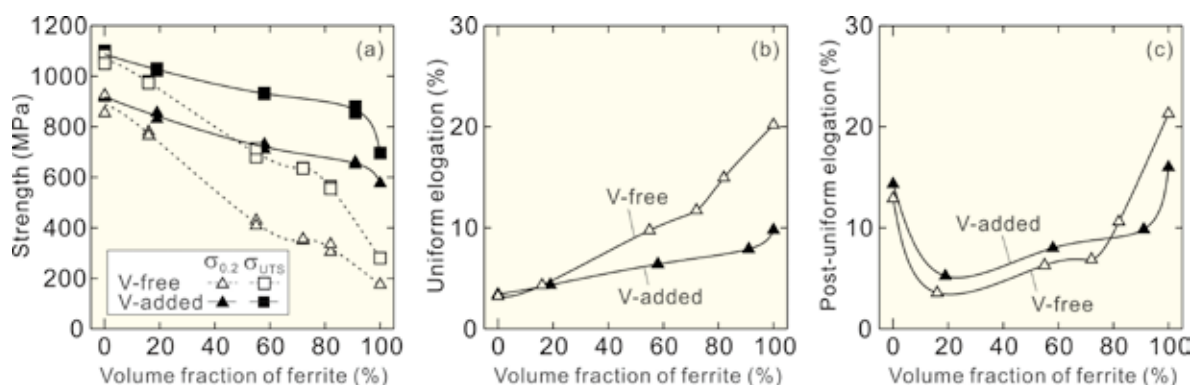


Fig. 1 Strength and ductility of V-free and V-added steels. (a) 0.2% proof stress and ultimate tensile strength, (b) uniform elongation and (c) post-uniform elongation.

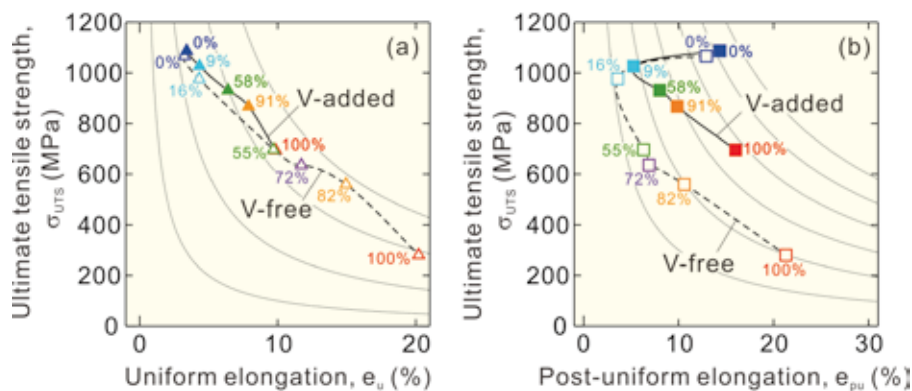


Fig. 2 Strength-ductility balance of V-free and V-added steels. (a) Ultimate tensile strength vs uniform elongation and (b) ultimate tensile strength vs post-uniform elongation.

V-added DP samples is higher than that of V-free DP samples, which should be due to precipitation strengthening of ferrite by nano-sized VC particles. Uniform elongation of the samples decreases by addition of vanadium, but post-uniform elongation is slightly larger in the V-added DP samples than that in the V-free samples.

Strength-ductility balance is compared between V-added and V-free samples in Fig. 2. The balance of ultimate tensile strength and uniform elongation in Fig. 2a shows that the balance curve is shifted toward high-strength and low-ductility region by V addition, but the balance of both V-added and V-free samples are located in the single curve. This result indicates that V addition increases the strength of DP samples with keeping a good balance of ultimate tensile strength and uniform elongation. On the other hand, it is clearly seen that V addition improves the balance of strength and post-uniform elongation in the DP samples.

To understand the difference in the mechanical properties of the DP samples between V-free and V-added steels, the work hardening behavior was compared. It was found that the work hardening rate during tensile test for ferrite-martensite DP samples decreases by addition of V. This can explain the reason why the uniform elongation decreased by addition of V. However, this result is somewhat surprising since nano-sized alloy carbides are reported to have an effect to increase the working hardening in the tensile test of single phase ferrite steels [3]. To further understand the mechanisms behind, digital image correlation (DIC)

analysis was applied to investigate the strain distribution introduced in the DP samples during tensile tests. The DIC analysis revealed the following results. In the V-free steel, strain distribution was quite heterogeneous, and in particular the strain was more concentrated on soft ferrite phase. However, it was clearly shown that the strain distribution became more uniform in the V-added steel. These tendencies suggest that precipitation strengthening of ferrite by VC particles reduces the difference in strength between ferrite and martensite phase in DP samples, which would suppress inhomogeneous deformation during the tensile test. This corresponds well with the decreased work hardening and smaller uniform elongation in the V-added DP samples. More homogeneous deformation caused by VC dispersion may also suppress formation of voids or cracks in the later stage of tensile deformation. This would be the reason why the V addition led to an increase in the balance of strength and post-uniform elongation. It can be suggested that nano-sized alloy carbides are effective for improving the post-uniform elongation as well as increasing the strength of DP steels.

References

- [1] "Fundamentals of Dual Phase Steels", edited by R. A. Kot and B. L. Bramfitt, AIME, (1981).
- [2] Y. Funakawa, T. Shiozaki, K. Tomita, T. Yamamoto, and E. Maeda: ISIJ International, **44**, 1945-1951(2004).
- [3] N. Kamikawa, Y. Abe, G. Miyamoto, Y. Funakawa, and T. Furuhashi: Tetsu-to-Hagane, **99**, 352-361(2013).

Keywords: steel, mechanical properties, deformation

Tadashi Furuhashi, Goro Miyamoto, and Naoya Kamikawa (Microstructure Design of Structural Metallic Materials Division)

E-mail: furuhara@imr.tohoku.ac.jp

URL: <http://www.st-mat.imr.tohoku.ac.jp>

Structure of Hydrated Copper silicate gels

Hydrated copper silicate gel samples were prepared using the conventional sol-gel method and stock solutions whose Cu/Si molar ratios were different. The structures of the obtained gel samples were analyzed using X-ray diffraction and extended X-ray absorption fine structure (EXAFS) spectroscopy. A common medium-range structure similar to that of natural chrysocolla was produced in each gel sample. The local structure of chrysocolla is readily produced in during sedimentation from any solutions containing CuO and SiO₂ components.

Chrysocolla, Cu₂H₂(Si₂O₅)(OH)₄·nH₂O, is a secondary mineral that forms in the oxidized zones of copper deposits (Fig. 1). Because of the unique Cu/Si molar ratio for natural chrysocolla, it is reasonable to assume that the production of natural chrysocolla is associated with a regular chemical reaction during sedimentation from solutions containing copper and silica components, and understanding the mechanism of the mineralization of chrysocolla is expected to provide useful information on its cryptocrystalline structure. This prompted us to study the disordered structure of a synthetic analogue of chrysocolla prepared using the sol-gel method [1].

The sol-gel method and reagents CuSO₄·5H₂O and Si(OC₂H₅)₄ (TEOS) were used to prepare hydrated copper silicate gels with three different Cu/Si molar compositions. The Cu/Si molar ratios for the three obtained gel samples were 0.32, 0.83, and 1.61 (hereafter named Cu₁Si₂, Cu₁Si₁, and Cu₂Si₁, respectively).

The thermogravimetric (TG) curves for Cu₁Si₂, Cu₁Si₁, Cu₂Si₁, and natural chrysocolla show relatively smooth weight losses of 19.0, 22.0, 24.3, and 20.2%, respectively. The differential thermal analysis (DTA) curves for Cu₁Si₁ and natural chrysocolla show exothermic peaks at ~680°C, which correspond to thermal decomposition during the formation of crystalline CuO. Although exothermic peaks are not clearly shown in of the DTA curves for



Fig. 1 Chrysocolla from Chuquicamata, Chile.

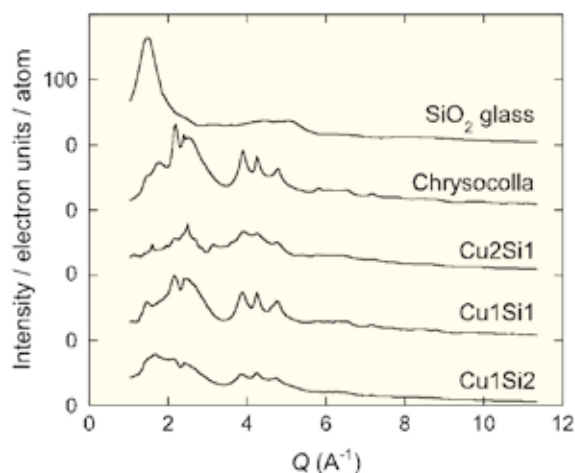


Fig. 2 X-ray diffraction patterns of three gel samples. The pattern of chrysocolla from Chuquicamata, Chile and SiO₂ glass are also shown.

Cu₁Si₂ and Cu₂Si₁, evidence of a similar reaction associated with the formation of CuO was found by heating Cu₁Si₂ and Cu₂Si₁ at 1000°C. This thermal behavior is different from that observed for Cu(OH)₂ (spertiniite). Therefore, each of the synthetic gel samples is not a simple assemblage of spertiniite and amorphous or crystalline silica but it also includes a substance similar to natural chrysocolla.

The X-ray diffraction (XRD) patterns for the three gel samples and for natural chrysocolla are shown in Fig. 2. Each pattern consists of a few diffuse maxima, and several broad peaks are superimposed on them. The profiles for Cu₁Si₂ and Cu₁Si₁ indicate broad peaks at $Q = 3.8, 4.2,$ and 4.6 \AA^{-1} , which correspond well with those for natural chrysocolla. In particular, the XRD pattern for Cu₁Si₁ is quite similar to that for natural chrysocolla, suggesting the Cu₁Si₁ gel is isostructural with natural chrysocolla. The first diffuse maximum in the XRD pattern for Cu₁Si₂, on the other hand, is attributed to the structure of ordinary amorphous SiO₂. This feature enables us to consider that part of the SiO₂ in Cu₁Si₂ is encouraged to form amorphous SiO₂.

Fig. 3 shows the reduced distribution functions (RDFs) for the Cu₁Si₂, Cu₁Si₁, and Cu₂Si₁ samples and for SiO₂ glass and natural chrysocolla. The atomic correlation peaks for every pair of constituents

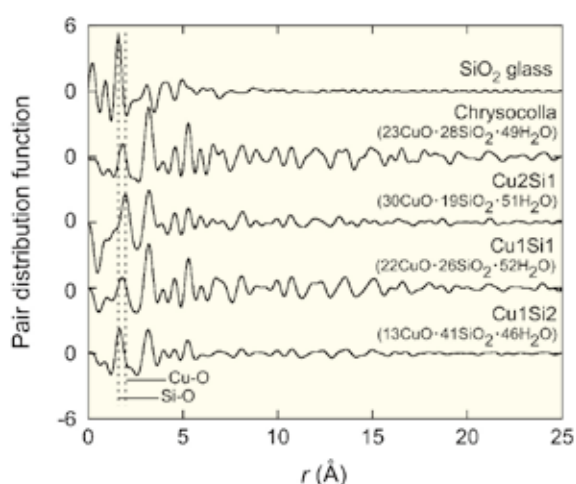


Fig. 3 Reduced atomic pair distribution functions of the gels, chrysocolla from Chuquicamata, Chile, and SiO_2 glass

are clearly observed up to ~ 15 Å for Cu_2Si_1 , Cu_1Si_1 , Cu_1Si_2 and natural chrysocolla. However, the atomic correlation for SiO_2 glass becomes less distinct with increasing radial distance and disappears over 10 Å. Since the oscillations in the reduced RDFs will represent the degree of structural ordering, the obtained Cu_1Si_2 , Cu_1Si_1 , and Cu_2Si_1 gel samples show structures whose middle-range orderings are different from those for common glasses. The dashed lines in Fig. 3 indicate the atomic distances for the Si-O bonds in the tetrahedral unit and the Cu-O bonds in the square planar unit, respectively. The first nearest-neighbor correlation for each gel represents a harmonization of the Si-O and Cu-O correlations and suggests the existence of the SiO_4 unit.

Fig. 4 shows Cu K -edge extended X-ray absorption fine structure EXAFS $\chi(k)$ functions for the synthetic gel samples and for natural chrysocolla. The spectra for Cu_1Si_2 , Cu_1Si_1 , and natural chrysocolla feature oscillation peaks at $k = 7.5$ and 10 Å^{-1} , while those peaks are absent in the spectrum for Cu_2Si_1 . This result indicates that the local structures around Cu in Cu_1Si_2 and Cu_1Si_1 are similar to that of natural chrysocolla and that Cu_2Si_1 has a unique Cu environment.

Copper silicate gels were synthesized through sol-gel precipitation from starting materials whose Cu/Si molar ratios were different. The TG-DTA, XRD, and EXAFS measurements indicated that middle-

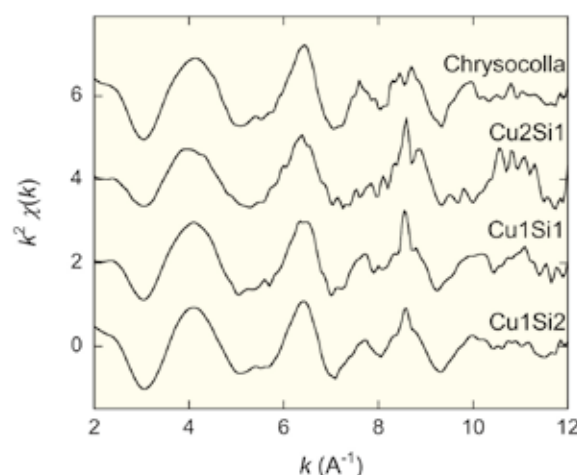


Fig. 4 Cu K -edge k^2 -weighted $\chi(k)$ functions of the gels and chrysocolla from Chuquicamata, Chile.

range ordering similar to that of natural chrysocolla was formed in each of the gel samples despite the variation in the Cu/Si molar ratio of the starting stock solutions. In particular, the structural feature of the Cu_1Si_1 gel sample is equivalent to that of natural chrysocolla. Therefore, the nearly stoichiometric composition of cryptocrystalline chrysocolla strongly associates with its short- and medium-range order, and this unique ordering is formed as a result of a chemical reaction during precipitation from solutions containing SiO_2 and CuO components. The local structural information about the CuO_4 units around Cu together with the common SiO_4 units observed in the Cu_1Si_1 gel and natural chrysocolla enables us to consider middle-range ordering such as that found in crystalline diopside ($\text{CaSiO}_3 \cdot \text{H}_2\text{O}$) and planchéite. However, the linkages of the CuO_4 and SiO_4 units in chrysocolla are still unknown. Further systematic investigation with methods such as high-energy X-ray diffraction is strongly required in order to obtain high-resolution pair distribution function data.

References

- [1] T. Hariu, H. Arima, and K. Sugiyama, *J. Mineral. Petrol. Sci.*, **108**, 111-115 (2013).

Keywords: cryptocrystalline, pair distribution function, XAFS

Hiroshi Arima, Kazumasa Sugiyama (Chemical Physics of Non-Crystalline Materials Division)

E-mail: arimah@imr.tohoku.ac.jp, kazumasa@imr.tohoku.ac.jp

URL: <http://www.xraylab.imr.tohoku.ac.jp/>

Improvement in Hard-Tissue Compatibility of β -type Titanium Alloy by Formation of Hydroxyapatite through Alkali Treatment and Metal Organic Chemical Vapor Deposition

The hard-tissue compatibility of the β -type Ti alloy Ti-29Nb-13Ta-4.6Zr (TNTZ) was improved using two methods. The effects of the alloying elements Ta, Nb, and Zr on the hydroxyapatite (HAp) formability of Ti alloys soaked in simulated body fluid after alkali treatment were investigated to improve the formability of HAp on TNTZ-based implants for the human body. Furthermore, the adhesive strengths of HAp films deposited through metal organic chemical vapor deposition onto TNTZ substrates were improved by controlling surface morphology of TNTZ substrates.

In biomedical applications, bone absorption and degradation of bone quality are induced by stress shielding resulting from mismatch between the Young's moduli of living bone tissue and implant devices. Therefore, a β -type Ti alloy, Ti-29Nb-13Ta-4.6Zr (mass%, TNTZ) [1], has been developed with a low Young's modulus to overcome this significant problem. The Young's modulus of TNTZ is approximately 60 GPa [1], which is much closer to that of cortical bone (10–30 GPa) than to those of existing Ti alloys. However, Ti and its alloys fuse with bone through fibrous tissues, and it takes a long time for them to do so [2]. Therefore, it is necessary to improve the hard-tissue compatibility of TNTZ.

A coating of hydroxyapatite ($\text{Ca}_{10}(\text{PO}_4)_6\text{OH}_2$; HAp) is very effective in improving the hard-tissue

compatibility of Ti and its alloys. HAp directly bonds with bone tissue without any fibrous cells forming. In the present study, two methods were used to form HAp on TNTZ in order to improve the hard-tissue compatibility of TNTZ.

The first method of forming HAp on the TNTZ surface is alkali treatment. HAp forms on the surfaces of pure Ti and its alloys immersed in a NaOH solution and then in simulated body fluid (SBF) whose ion concentrations are almost the same as those in the human body. However, the HAp formability of TNTZ soaked in SBF after alkali treatment is lower than that of pure Ti that has been subjected to the same treatment conditions. Therefore, it is important to understand the relation between the alloying elements Nb, Ta, and Zr and HAp formability in order to improve the HAp formability of TNTZ. In this study, the HAp formability of Ti-xM (nominal content $x = 10, 20, 30$, or 40 mass%; $M = \text{Nb, Ta, or Zr}$) and of each pure metal soaked in SBF after alkali treatment was investigated [3].

Fig. 1 shows scanning electron microscope (SEM) images of the surfaces of (a) Ti-xNb and pure Nb, (b) Ti-xTa and pure Ta, and (c) Ti-xZr and pure Zr soaked in SBF for 1 week after alkali treatment in 1 M NaOH solution at 363 K for 259.2 ks [3]. The HAp coverage on the Ti-xTa surfaces is almost constant at ~95%; however, the coverage on the Ti-xNb and Ti-xZr surfaces decreased from 90–95% to 0% as the Nb and Zr contents increased from 10 to 100 mass% (*i.e.*, pure Nb and Zr metals).

The X-ray diffraction (XRD) profiles for the alkali-treated Ti-xTa showed that $\text{Na}_2\text{Ti}_5\text{O}_{11}$ and Na_5TaO_5 had formed on the surfaces (data not shown here) [3]. The XRD profiles for the alkali-treated Ti-xNb and Ti-xZr, on the other hand, showed that only $\text{Na}_2\text{Ti}_5\text{O}_{11}$ had formed on the surfaces (data not shown here) [3]. The Ti-Nb and Ti-Zr alloys showed good HAp formability when the Nb and Zr contents were lower than 10 mass% because enough sodium titanate was present on the surfaces. However, when the Nb or Zr content was increased to 20 mass%, the number of Ti atoms on the surfaces decreased, resulting in a

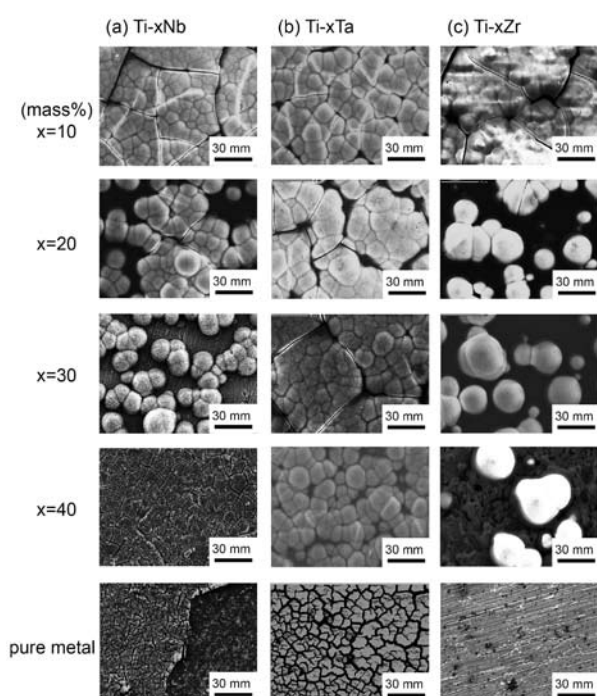


Fig. 1 SEM images of Ti-xM (nominal content $x = 10, 20, 30$, or 40 mass%; $M = \text{Nb, Ta, or Zr}$) alloy and each pure metal soaked in SBF for 1 week after alkali treatment in 1 M NaOH solution at 363 K for 259.2 ks.

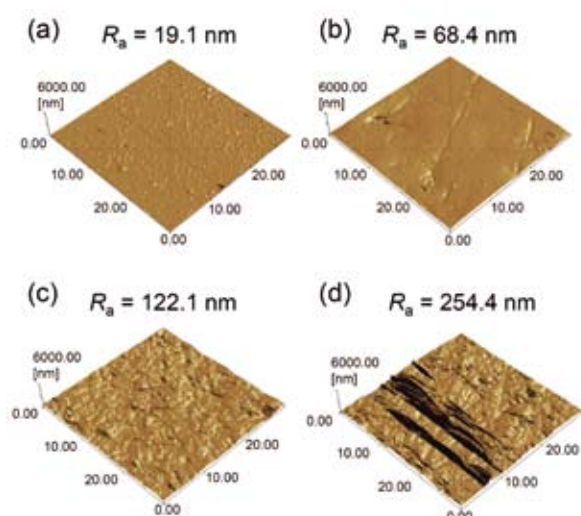


Fig. 2 AFM images of (a) TNTZ substrate surface with mirror-like finish and TNTZ substrates polished with (b) #2400-, (c) #1500-, and (d) #1000-grit abrasive papers.

decrease in the sodium titanate content on the surfaces. These results suggest that the sodium titanate and sodium tantalate on the surfaces were responsible for HAp nucleation. Therefore, it is important to maximize the formation of sodium titanate and sodium tantalate on the TNTZ surface in order to improve the hard-tissue compatibility of TNTZ.

The second method of forming HAp on the TNTZ surface is dry coating; namely, metal organic chemical vapor deposition (MOCVD), which is a useful method of coating HAp films onto metal surfaces. This study was undertaken with the aim of improving the adhesive strength of HAp films deposited onto TNTZ substrates through MOCVD by optimizing the surface morphology; *i.e.*, the surface roughness and size of asperities of the TNTZ substrates [4].

Fig. 2 shows atomic force microscopy (AFM) images and surface roughness (R_a) values for TNTZ substrates with a mirror-like surface finish and for those polished with #1000-, #1500-, and #2400-grit abrasive papers [4]. The surfaces of the TNTZ substrate with a mirror-like finish and that polished with #2400-grit abrasive paper are relatively smooth. The surfaces of the TNTZ substrates polished with #1500- and #1000-grit abrasive papers, on the other hand, are uniformly rough and show nanoasperities. Microasperities are also observed on the surface of the TNTZ substrate polished with

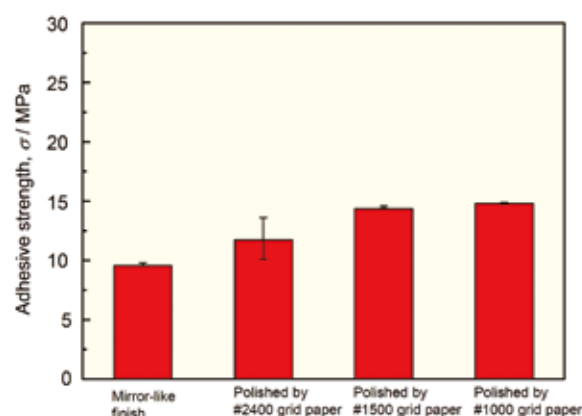


Fig. 3 Adhesive strengths of HAp films deposited onto TNTZ substrate with mirror-like surface finish and TNTZ substrates subjected to mechanical polishing using #2400-, #1500-, and #1000-grit abrasive papers.

the #1000-grit abrasive paper.

Fig. 3 shows the adhesive strengths of the HAp films deposited onto the TNTZ substrate with a mirror-like surface finish and onto those whose surfaces were polished with #1000-, #1500-, and #2400-grit abrasive papers [4]. The adhesive strength of the HAp film deposited onto the TNTZ substrate with a mirror-like surface finish is approximately 10 MPa. Mechanical polishing using #1000-, #1500-, and #2400-grit abrasive papers improved the adhesive strengths of the HAp films. The surface of the TNTZ substrate polished with the #1000-grit abrasive paper is rougher than that of the TNTZ substrate polished with the #1500-grit abrasive paper. However, the adhesive strengths of the HAp films deposited onto these two substrates are nearly equal. These results indicate that the nanoasperities play a more important role in improving the adhesive strength of the HAp films than the surface roughness of the substrates does.

References

- [1] D. Kuroda, M. Niinomi, M. Morinaga, Y. Kato, and T. Yashiro, *Mater. Sci. Eng. A* **243**, 244 (1998).
- [2] M. Niinomi, T. Hattori, K. Morikawa, T. Kasuga, A. Suzuki, H. Fukui, and A. Niwa, *Mater. Trans.* **43**, 2970 (2002).
- [3] K. Cho, M. Niinomi, M. Nakai, J. Hieda, and X. Tao, *Mater. Trans.* **54**, 1295 (2013).
- [4] J. Hieda, M. Niinomi, M. Nakai, K. Cho, T. Gozawa, H. Katsui, R. Tu, and T. Goto, *J. Mech. Behav. Biomed. Mater.* **18**, 232 (2013).

Impurity Partitioning During Colloidal Crystallization

Colloidal crystal was used as a model of impurity partitioning during the growth of a bulk crystal. The detailed partitioning behavior of the colloidal crystal was investigated for the first time. The effective partition coefficient, k_{eff} ($= C_s/C_0$), was investigated for pure polystyrene and for polystyrene dyed with fluorescent particles by changing the ratio of the particle diameters, $D_{\text{imp}}/D_{\text{cryst}}$, and growth rate, V . k_{eff} was less than unity and increased to unity with increasing V for each size of polystyrene particles, whereas k_{eff} increased to unity as $D_{\text{imp}}/D_{\text{cryst}}$ approached unity at a given growth rate. These results were consistent with the solute behavior analyzed using a Burton-Prim-Slichter (BPS) model. The equilibrium partition coefficient, k_0 , obtained from the BPS plot increased as $D_{\text{imp}}/D_{\text{cryst}}$ approached unity. In contrast, although the fluorescent particles also followed the BPS model, they showed higher k_0 values than the counterpart polystyrene particles did. k_0 values greater than unity were obtained for the impurities whose sizes were similar to that of the host particles. This behavior is attributed to the positive free energy of fusion associated with incorporating the fluorescent particles into the host matrix. Such positive free energy of fusion implies the presence of the enthalpy associated with the interactions among the particles.

Colloidal crystals are a promising tool for investigating diverse basic physical phenomena. We applied a colloidal crystal to impurity partitioning because impurity partitioning is one of the most universal phenomena observed during the growth of crystals from melts, and it strongly affects the properties of bulk crystals. Since no research has previously been conducted on the impurity partitioning of colloidal crystals, this work investigates the detailed partitioning behaviors such as the growth rate, size of impurity particles, and types of impurities formed during colloidal crystallization [1].

A small amount of impurities (2%) was doped

into a colloidal dispersion from which colloidal crystals were grown. Various sizes of pure polystyrene (PS) particles (*i.e.*, 300, 400, 600, and 700 nm) and fluorescent bearing (w/fluor.) particles (*i.e.*, 300, 400, 520, 600, and 700 nm) were doped as impurity particles into the colloidal crystals.

Convective assembly [2] was used to grow the colloidal crystals. More than several tens of layers of colloidal crystals were formed on a glass plate (Fig. 1A). The cleavage surface was observed using scanning electron microscopy (SEM) to evaluate the concentrations of the impurity particles in the bulk. Most of the impurity particles had substituted for constituent particles, as shown in Fig. 1B.

The effective partition coefficient (k_{eff}) was measured at various growth rates (Fig. 1C) and for each size of each impurity particle. k_{eff} approached unity with increasing growth rate for each sample. Further, the closer the size of the impurity particle was to that of the host particle, the easier it became for k_{eff} to approach unity. In addition, the k_{eff} values for the w/fluor. particles were larger than those for the pure PS particles for all particle sizes. It should also be noted that k_{eff} for the 520 nm w/fluor. particles surpassed unity.

Fig. 1D shows k_0 obtained from k_{eff} by using BPS plot [3]. k_0 decreased with increasing difference between the size of the impurity particle and the 500-nm host particle. k_0 for each w/fluor. particle size was larger than that for the corresponding pure PS particle size. k_0 surpassed unity for the 520-nm w/fluor. particle, whereas it was always less than unity for the PS particles.

We used a Thurmond and Struthers (T&S) model [4] to determine the difference between the k_0 values for the PS and w/fluor. particles. The T&S model defines k_0 as $\exp((\Delta G_{\text{Tr}} - \Delta H)/RT)$, where ΔG_{Tr} is the change in the Gibbs free energy of fusion; that is, the difference between the Gibbs free energies of the solid and liquid phases of an impurity at the

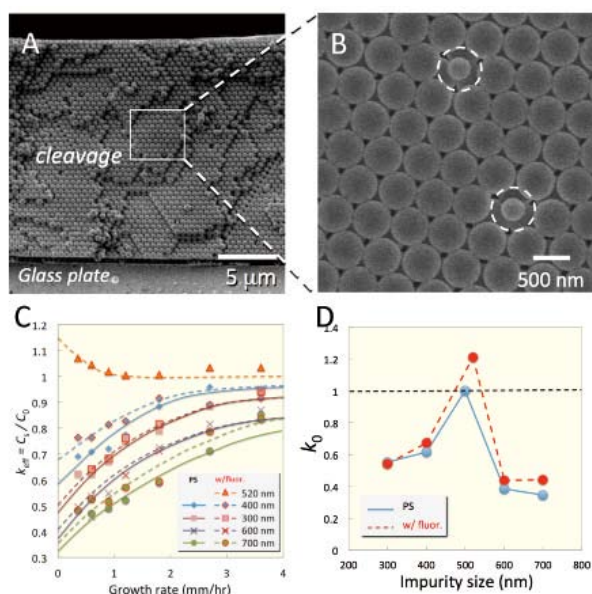


Fig. 1 **A.** Few tens of layers of colloidal crystals grown using convective assembly. Cleavage surfaces were observed using SEM to obtain concentration of impurity particles in solid (C_s). **B.** Impurity particles substituted for constituent particles. **C.** Effective partition coefficients (k_{eff}) for various sizes of PS and w/fluor. particles. **D.** Equilibrium partition coefficients (k_0) for PS and w/fluor. particles.



transition temperature, T , ΔH is the excess enthalpy produced by incorporating the impurity into the host material, and R is the gas constant. During typical crystal growth, ΔG_{Tr} is obtained at the transition temperature of the host material. The volume fraction, ϕ , which is the total particle volume divided by the total system volume, on the other hand, is used as a parameter for the phase transition of the colloidal dispersion into a colloidal crystal during colloidal crystal growth. It is necessary to investigate the volume fraction of the phase transition, ϕ_{Tr} , for two different types of impurities in order to evaluate ΔG_{Tr} and k_0 for both impurities.

The value of ϕ_{Tr} was determined using the number densities and effective diameters of the particles. The effective diameter is the sum of the real radius of the particle and the additional portion owing to the thickness of the electrical double layer, which was obtained by measuring the zeta potential of each impurity particle. The number density was measured using optical microscopy by counting the number of particles in the liquid phase, which coexists with the solid phase. Consequently, the ϕ_{Tr} value for w/fluor. was less than that for PS for each particle size.

Fig. 2A shows a schematic of the molar Gibbs free energy curves for the PS and w/fluor. particles. The molar Gibbs free energy is obtained by plotting the Gibbs free energy as functions of the mole fractions, x , of the colloidal particles. We used the free energy curve to represent a binary system even though the colloid only had one component. Counter end members are thought to be vacancy (left direction) and colloidal particles (right direction), which are assumed to be at lattice points in both the liquid and solid phases. From the diagram, the chemical potentials of the solid and liquid phases can be obtained from the lines tangent to the curves.

We will now discuss why k_0 for w/fluor. is larger than that for PS. The molar free energy curve for the PS impurity is the same as that for the host because the materials are the same (Figs. 2A(a) and (b)). Since the ϕ_{Tr} for PS and that for the host are the same, which corresponds to the same mole fraction, the change in the free energy of the PS, $\Delta G_{Tr} (= \mu_L - \mu_S)$, is zero. This is because the common tangent lines are the same for the host and the impurity. In contrast, ΔG_{Tr} is positive for w/fluor. (Fig. 2A(c))

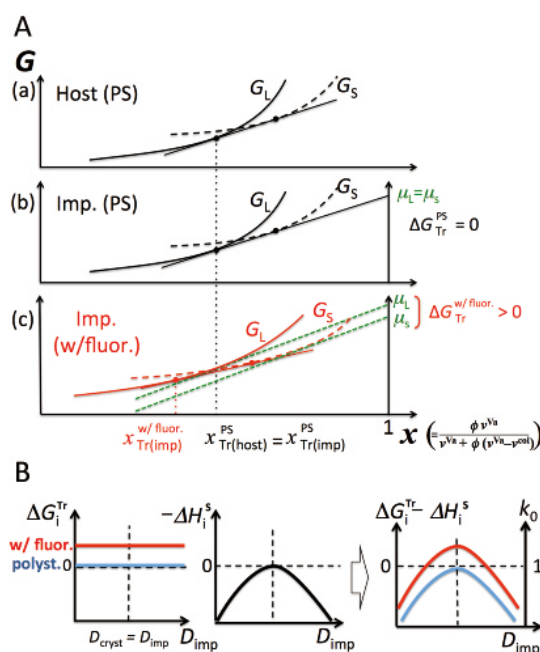


Fig. 2 **A.** Gibbs free energy plotted as functions of mole fractions of host PS crystals and of PS and w/fluor. impurity particles. **B.** k_0 obtained from ΔG_{Tr} and ΔH for PS and w/fluor. particles.

because the w/fluor. particle is smaller than the host PS particle.

Therefore, $\Delta G_{Tr} - \Delta H$ is larger for w/fluor. than it is for PS, which corresponds to a larger k_0 for w/fluor. than for PS, and k_0 for w/fluor. surpasses unity in a small $-\Delta H$ range (Fig. 2B).

The different types of impurity particles had different k_0 values, which is attributed to the difference in their ϕ_{Tr} values. We have explained impurity partitioning during colloidal crystallization by applying the BPS and T&S models.

References

- [1] J. Nozawa, S. Uda, Y. Naradate, H. Koizumi, K. Fujiwara, A. Toyotama, and J. Yamanaka, *J. Phys. Chem. B* **117**, 5289 (2013).
- [2] P. Jiang, J. F. Bertone, K. S. Hwang, and V. L. Colvin, *Chem. Mater.* **11**, 2132 (1999).
- [3] J. A. Burton, R. C. Prim, and W. P. Slichter, *J. Chem. Phys.* **21**, 1987 (1953).
- [4] C. D. Thurmond and J. D. Struthers, *J. Phys. Chem.* **57**, 831 (1953).

Cobalt- and Titanium-based Alloys for Biomedical and Industrial Applications

Co-Cr-Mo (CCM) alloys are commonly used for artificial hip- and knee-joint prostheses. We studied the deformation and corrosion behaviors of CCM alloys for biomedical and industrial applications. In addition, conventional ultrafine-grained Ti-6Al-4V alloy exhibited low-temperature, high-strain-rate superplasticity.

The mechanical behaviors of Co-Cr-Mo (CCM) alloys are dominated by strain-induced martensitic transformation (SIMT), which not only initiates cracks during plastic deformation but also dramatically enhances the wear resistance of CCM alloys in practical use. It is essential to clarify the factors that affect SIMT in order to develop more reliable CCM alloys. In this study [1], we focused on the effect of annealing twin boundaries (ATBs) on SIMT behavior. We analyzed in detail the substructures that had formed near a parallel pair of ATBs after deformation under a stress preferable for a slip parallel to the ATBs. Scanning electron microscopy/electron backscatter diffraction (SEM-EBSD) and transmission electron microscopy (TEM) were used to find the

preferential formation of an ϵ -HCP (hexagonal close-packed) phase at ATBs in a metastable γ -FCC (face-centered cubic) phase. High-resolution TEM (HRTEM) images (Fig. 1) indicated that the ϵ -HCP phase did not regularly thicken on every second atomic plane, which would form the perfect HCP-structured ϵ -phase but irregularly left a high density of stacking faults. Furthermore, the thickness of the ϵ -HCP phase was different at ATBs on both sides of the twin. The results of the residual stress analysis based on the EBSD-Wilkinson method and the results of the phase-field simulation of solute segregation at ATBs suggest that the difference in the thicknesses was attributed to the internal stress due to strain incompatibility at the ATBs. More reliable biomedical CCM alloys can be developed based on these results.

Co-based alloys can also be used as materials in Al die-casting. The fundamental behaviors of the interfacial reactions between solid Co and Fe on the one hand and liquid Al on the other were compared by observing the interface structures and by analyzing the reaction kinetics [2], which laid a foundation for elucidating the mechanisms for the interfacial reactions between Co-based and Fe-based alloys on the one hand and liquid Al on the other. Interface structures typical for solid Co and Fe that had previously been immersed in liquid Al are shown in Figs. 2(a) and (b), respectively. According to the results of the electron probe microanalysis (EPMA) and the Co-Al binary phase diagram, the intermediate layers close to the Al phase and to the Co matrix were identified as the Co_2Al_9 and Co_2Al_5 intermetallic compounds, respectively. It is assumed that all of the Co_2Al_9 formed during cooling and that only a single Co_2Al_5 layer formed during the interfacial reactions. Similarly, we believe that only $\text{FeAl}_{2.8}$ inner layers formed during the interfacial reaction between the solid Fe and liquid Al. A general model was constructed based on this assumption, as shown in Fig. 2(c), for the interfacial reactions. The solid metal (either Co or Fe) and liquid Al came into contact with one other when the solid metal was immersed into the liquid Al, as shown in Fig. 3(c). The two different metals then reacted at their interface and formed a continuous layer of an intermetallic compound (Fig. 2(d)). Al atoms that diffused through the intermetallic layer at the interface between the solid metal and the intermetallic compound (*i.e.*, at interface I) then

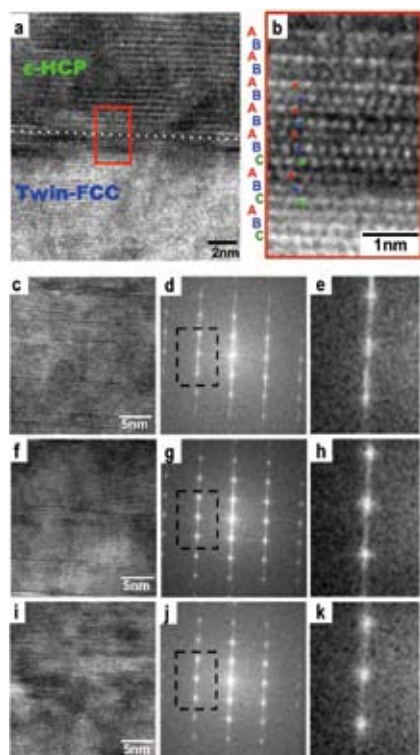


Fig.1 High-resolution transmission electron microscope (HRTEM) images of the twin-containing CCM-alloy deformed to 8% plastic strain. (a) ϵ -HCP/Twin-FCC interface. (b) Magnified image of the area indicated by a red rectangular in (a). (c), (f), (i) are HRTEM images of the upper (*i.e.* near M1), middle, and lower (*i.e.* near Twin) regions of the ϵ -HCP plate. (d), (g), (j) are the Fourier transformed patterns of (c), (f), (i), respectively. (e), (h), (k) are the magnified images of the area indicated by dashed rectangular in (d), (g), (h), respectively.

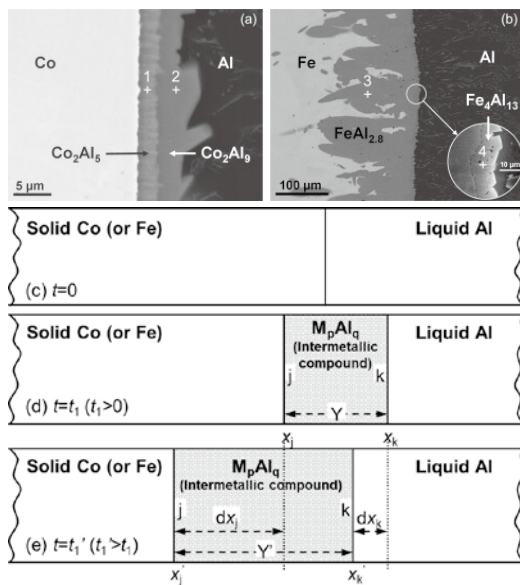


Fig. 2 Interface structure in cross section after immersion test at 1013 K for 3600 s.

reacted with the solid metal and formed more intermetallic compound, causing interface I to move toward the solid metal side of the interface because some of the solid metal was consumed during the reaction. The intermetallic layer, on the other hand, was unstable in the liquid Al and dissolved into it through the interface between the intermetallic compound and the liquid Al (*i.e.*, through interface II), causing interface II to move toward the solid metal side of the interface (Fig. 2(e)). The decrease in the thickness of the solid metal is obviously due to the movement of interface I, and the change in the thickness of the intermetallic compound is the result of the relative motions of interfaces I and II.

Further, the Ti-6Al-4V alloy used in this study exhibited low-temperature, high-strain-rate superplasticity [3]. The mechanism for the conversion of the initial α' -martensite microstructure during hot deformation (at 973 K-10 s⁻¹) of the Ti-6Al-4V alloy was studied based on detailed microstructural observations, kinetic analysis of the deformation of the microstructure, and various theoretical models. The initial α' -microstructure was compressed at 973 K-10 s⁻¹ and at a height strain of 0.8. The initial α' -microstructure whose morphology was acicular evolved into an ultrafine-grained microstructure whose grains were an average of 0.2 μm in diameter and that showed a large fraction of high-angle grain

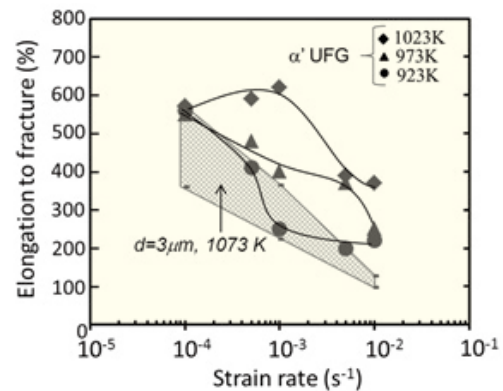


Fig 3 Elongation to fracture of new type of UFG-Ti-6Al-4V alloy (α' -UFG) as compared to the result of Ti-6Al-4V alloy with grain size of 3 μm as a function of initial strain rate.

boundaries. The formation of martensite-variant subgrains and new high-angle-boundary grains located at the interfaces of the martensite variants and {10-11} twins dominated during the initial stage of deformation. Discontinuous dynamic recrystallization (DDRX) and heterogeneous nucleation and fragmentation of the high-angle-boundary grains dominated when the height strain was increased to 0.8. In contrast, continuous dynamic recrystallization (CDRX) dominated throughout deformation when the initial microstructure was ($\alpha+\beta$). Thus, DDRX becomes dominant when the initial microstructure is changed from the conventional ($\alpha+\beta$) microstructure to the acicular α' -martensite one. This behavior of the α' -martensite microstructure is attributed to the numerous nucleation sites such as dislocations, to the interfaces between the martensite variants and {10-11} twins, and to the high-speed grain fragmentation and subgrain formation in the initial α' -martensite microstructure during the initial stage of deformation. Furthermore, the Ti-6Al-4V alloy whose ultrafine-grained microstructure was produced using this method of processing exhibited low-temperature, high-strain-rate superplasticity.

References

- [1] Y. Koizumi, S. Suzuki, K. Yamanaka, B. S. Lee, K. Sato, Y. Li, S. Kurosu, H. Matsumoto, and A. Chiba, *Acta Materialia* **61**, 1648-1661 (2013).
- [2] T. Tang, Y. Li, S. Kurosu, Y. Koizumi, H. Matsumoto, and A. Chiba, *Corros. Sci.* **60**, 32-37 (2012).
- [3] H. Matsumoto, K. Yoshida, S. H. Lee, Y. Ono, and A. Chiba, *Mater. Lett.*, **98**, 209-212 (2013).

Atomic-Resolution Analysis of Diffusional-Displacive Transformation of Long-Period Stacking Order phases in Mg₉₇Zn₁Y₂ Cast Alloys

The phase transformation of the long-period stacking order (LPSO) structure in aged Mg₉₇Zn₁Y₂ alloys was investigated using aberration-corrected high-angle angular dark field scanning transmission electron microscopy (HAADF-STEM). The transformation occurs through a mechanism resembling diffusional-displacive phase transformation. Local strain analysis on the basis of HAADF-STEM images was used to elucidate that the lattice spacing of the (0001)_{Mg} planes in the face-centered cubic (FCC)-type enrichment layer is shorter than that in the hexagonal close-packed (HCP)-type transition region. These structural and compositional irregularities are elementary in the transformation of the LPSO structure in Mg₉₇Zn₁Y₂ alloys.

Magnesium (Mg)-based alloys have attracted much attention as next-generation lightweight structural materials because of their low density, high specific strength, damping capacity, recycling efficiency, and other features. A series of novel structures that show so-called “synchronized long-period stacking order (LPSO)” in Mg-TM-RE alloy systems (where “TM” and “RE” denote transition metal and rare earth) has recently been reported [1]. Synchronized LPSO signifies the segregation of TM and RE elements into stacking faults and the long-range ordering of the segregated stacking faults.

The Mg₉₇Zn₁Y₂ alloy shows 0.2% proof strength higher than 600 MPa and an elongation of 5% [1]. Many researchers have previously examined the atomic-level structure of the LPSO. The 10H, 14H, 18R, and 24R polytypes are found in the Mg-Zn-Y alloy, depending on the thermal history of the alloy and the concentration of solute in the alloy [2, 3].

Although the formation and growth mechanism of the LPSO have not been elucidated in a long time, Zhu *et al.* recently proposed a mechanism for the transformation from the 18R- to the 14R-type LPSO structure in Mg_{96.7}Zn_{0.8}Y_{2.4}Zr_{0.2} alloys [4]. They also showed that the 24R-type irregularity plays a role in the transformation. However, they did not consider modulations in composition and structure at ledges, nor did they consider the change in the sequence of the LPSO with the 24R-type irregularity in Mg_{96.7}Zn_{0.8}Y_{2.4}Zr_{0.2} alloys aged for different lengths of time.

We examined the transition state from the perspectives of structural and compositional irregularities in the LPSO in Mg₉₇Zn₁Y₂ alloys. The irregularity of the LPSO structure in aged Mg₉₇Zn₁Y₂ alloys was examined using aberration-corrected high-angle annular dark field scanning transmission electron microscopy (HAADF-STEM) and peak-pair analysis (PPA) [5].

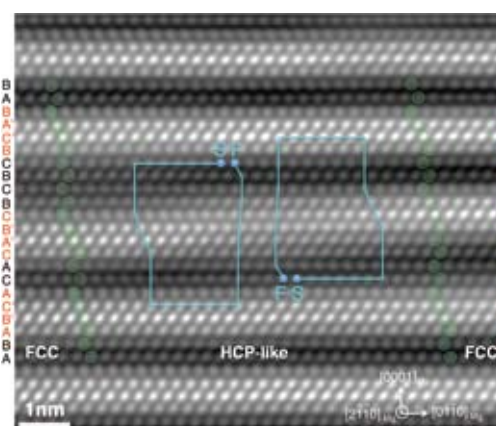


Fig. 1 HAADF-STEM image taken around transition region between 18R- and 24R-type periodicity in LPSO band. Stacking sequence in transition region changes from FCC to HCP-like stacking, which is incomplete HCP stacking.

Modulations in composition and structure in and around transition region [6]

Fig. 1 shows a Bragg-filtered HAADF-STEM image taken around a transition region in an LPSO band. Two Burgers circuits clearly show that a pair of Shockley partial dislocations with $\mathbf{b} = 1/3[01\bar{1}0]$ and $\mathbf{b} = 1/3[0110]$ exist at both sides of the hexagonal close-packed (HCP)-like region. These partial dislocations indicate the existence of a pair of ledge structures. However, the structure gradually changes from a face-centered cubic (FCC) structure to an HCP-type one. The structure in the transition region seems to be a strained HCP-type structure. The A' stacking layer moves by the two close-packed (0001)_{Mg} planes across the transition region; the stacking order locally changes from left to right B'→C, C→A', B→B'. Here, A', B', and C' denote solute enrichment layers with different stacking planes in an FCC-type stacking sequence. The Z²-contrast of the transition region is lower than that of the normal enrichment layer of an FCC-type stacking sequence, meaning that the solute elements can easily migrate across (0001)_{Mg} planes in the transition region.

Consequently, the LPSO structure would change through a type of diffusional-displacive transformation [7].

Local strain around the transition region [6]

Fig. 2 shows (a) an HAADF-STEM image and (b–d) show strain mappings around the transition region of an enrichment layer obtained from the PPA of the HAADF-STEM image. Here, the strain was measured relative to the lattice spacing of the nonenrichment layer. The in-plane normal strain map in Fig. 2(b) shows homogeneous contrast with an accuracy of $\pm 0.3\%$, which means that the interface between the enrichment layer and the nonenrichment layer is actually coherent. The out-of-plane normal strain map in Fig. 2(c) shows that the lattice spacing of the enrichment layer is 16% smaller than that of the nonenrichment layer. The strain is limited to within the enrichment layer including a transition region (layer (2)) and the neighboring two nonenrichment layers (layers (1) and (3)). The lattice spacing within the transition region is about 12% smaller than that in the nonenrichment layer. The simple shear strain map in Fig. 2(d) also shows a feature similar to that shown in Fig. 2(c). The signs of the strain in the enrichment layers are identical and positive, meaning that the LPSO is R-type and that the $(01\bar{1}0)$ planes tilt to the right.

These strain maps indicate that the strain in the transition region gradually decreased with decreasing Z^2 -contrast; *i.e.*, with decreasing concentration of the solute elements. Figs 2(c) and (d) also show that the enrichment layers are separated in the transition layer. On the basis of these results, a schematic model such as that shown

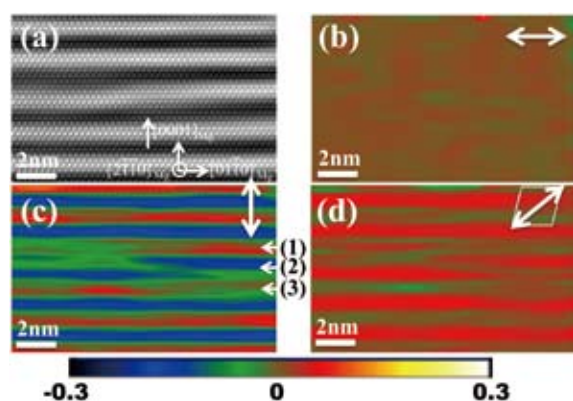


Fig. 2 (a) HAADF-STEM image and (b–d) strain mapping around transition region of enrichment layer. (b) In-plane normal strain, (c) out-of-plane normal strain, and (d) simple shear strain.

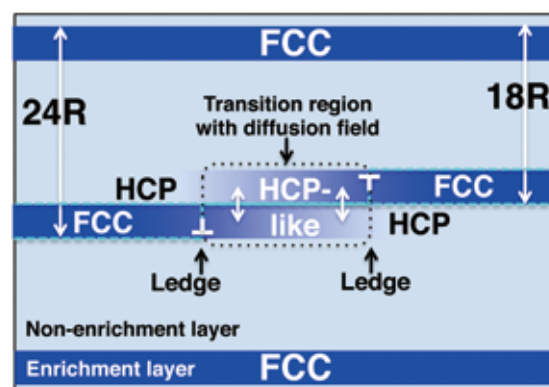


Fig. 3 Schematic model for transformation of LPSO through transition region.

in Fig. 3 can be proposed for the region around the transition layer. The stacking sequences are HCP- and FCC-type, inside and outside the transition region, respectively. Shockley partials exist in ledges between those stacking sequences. The HCP-like transition regions in front of two ledges fuse together and form a kind of diffusion field through which the solute elements easily migrate without changing the stacking sequence in the out-of plane direction of the LPSO; the diffusion field in front of the ledge serves as a buffer for the short-range migration of solute elements. The transition region subsequently moves in a $[01\bar{1}0]_{Mg}$ or $[0\bar{1}10]_{Mg}$ direction on the $(0001)_{Mg}$ planes accompanying the movement of a pair of partial dislocations. The strain accompanied with the transformation is localized around a transition region. Consequently, the enrichment layer grows or shrinks in the $[01\bar{1}0]_{Mg}$ or $[0\bar{1}10]_{Mg}$ direction, which is the elementary step in the phase transformation of LPSO.

References

- [1] Y. Kawamura, K. Hayashi, A. Inoue, and T. Masumoto: Mater. Trans. **42**, 1172 (2001).
- [2] E. Abe, Y. Kawamura, K. Hayashi, and A. Inoue: Acta Mater. **50**, 3845 (2002).
- [3] E. Abe, A. Ono, T. Itoi, M. Yamasaki, and Y. Kawamura: Philos. Mag. Lett. **91**, 690 (2011).
- [4] Y. M. Zhu, A. J. Morton, and J. F. Nie: Acta Mater. **60**, 6562 (2012).
- [5] E. Abe, A. Ono, T. Itoi, M. Yamasaki, and Y. Kawamura: Philos. Mag. Lett. **91**, 690 (2011).
- [6] T. Kiguchi, Y. Ninomiya, K. Shimmi, K. Sato, and T. J. Konno: Mater. Trans. **54**, 668 (2013).
- [7] J. W. Christian: Metallur. Mater. Trans. A **25**, 1821 (1994).

First-Principles Study of Interface Structure and Energy of Iron/Niobium Carbide

The Computational Materials Research Initiative (CMRI) was established as a project-oriented section at the Institute for Materials Research (IMR) in 2011 and is currently one of the three institutions operating under the Computational Materials Science Initiative (CMSI) founded through a Grant for Field 2 “New Materials and Energy Creation” of the High-Performance Computing Infrastructure (HPCI) Scientific Program of the Ministry of Education, Culture, Sports, Science, and Technology. As of May 2013, thirty-one researchers and supporting staff from universities, government organizations, and companies all over Japan are participating in CMRI along with the other two CMSI operating institutions, the Institute for Solid-State Physics (at The University of Tokyo) and the Institute for Molecular Science (at the National Institutes of Natural Sciences). CMRI conducts various programs of computational materials science. Among the seven Priority Research Topics of CMSI for which machine time is prioritized for using the K computer to accelerate the progress of calculations, CMRI has been pursuing research entitled “Development of multiscale structural design and assessment techniques to improve the performance of metallic structural materials.” The task group committed to this research is headed by Dr. M. Kohyama, AIST, and several CMRI members are also actively involved. Introduced below is a summary of one of the major outcomes obtained by Dr. H. Sawada, one of the core members of CMRI, and his coworkers [1]. They performed the so-called $O(N)$ Krylov-subspace method of calculating electronic structures from first principles to clarify the key factors for controlling the growth of precipitates in steel. A classical molecular dynamics simulation was also performed to estimate the amount of strain energy around the precipitates.

The size and density of precipitates are important factors in controlling the strength and toughness of steel. It is necessary to know the number of nucleation sites, the diffusivity of solute atoms, and the amount of interface energy between iron and the precipitates in order to predict the size and density of the precipitates. An attempt was made for the first time at using the $O(N)$ Krylov-subspace method of calculating electronic structures from first principles [2] instead of using the conventional diagonalization method to directly determine the interface energies of the semicoherent interfaces between body-centered cubic (bcc) iron and niobium carbide (NbC) arranged in a lattice containing more than 1000 atoms. An attempt was also made at using classical molecular dynamics (MD) simulation to calculate the strain energy in

order to estimate the size of the precipitate at the transition from a coherent precipitate to a semicoherent one.

Two examples of a coherent interface were calculated. In one case, a C atom existed on top of an Fe atom at the interface and in the other, an Nb atom existed on top of an Fe atom. These calculations were performed for a unit cell consisting of 7 Fe and 7 NbC layers, and the interface energy was defined as the difference between the total energy of the system including the interface and the sum of all the energies of the individual phases. As shown in Fig. 1, the interface formed when the C atom is on top of the Fe atom is more stable than the interface formed when the Nb atom is on top of the Fe atom. In addition, the interface separation in the former case is shorter than that in the latter one.

The semicoherent interface consists of m units of bcc iron and n units of NbC along the [100] and [010] directions. The lattice constant of NbC, $a_0(\text{NbC})$, is $1/\sqrt{2}$ of the conventional lattice constant because of the Baker-Nutting orientation relation. The misfit, ε , between the bcc iron and NbC phases for a semicoherent interface,

$$\varepsilon = |m \times a_0(\text{Fe}) - n \times a_0(\text{NbC})| \quad (1)$$

was minimized to 0.03 Å by choosing 9 and 8 for m and n , respectively. Here, $a_0(\text{Fe})$ and $a_0(\text{NbC})$ are the lattice constants of bcc iron and NbC. Lengths a_0 and b_0 of the unit cell for the semicoherent interface were fixed at $n \times a_0(\text{NbC})$. The calculation was performed for a 14-layer unit cell consisting of 7 Fe and 7 NbC layers along the [001] direction. The interface energy calculated for the semicoherent

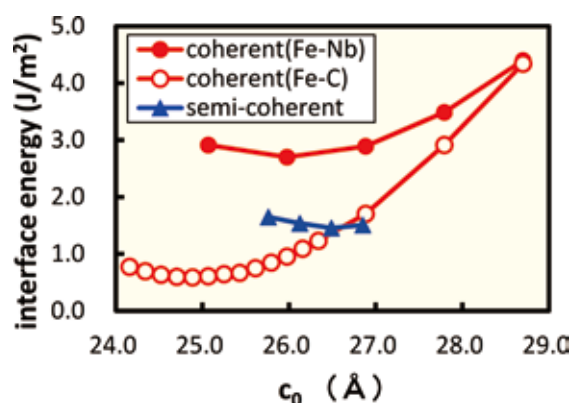


Fig. 1 Interface energies calculated for coherent and semicoherent interfaces between bcc iron and NbC and plotted as functions of length of c_0 .



interfaces is between those for the two coherent interfaces, as shown in Fig. 1. The separation of the semicoherent interface, however, is close to that of the coherent interface when the Nb atom exists on top of the Fe atom.

Fig. 2 shows the optimized atomic positions of the semicoherent interface in the (110) plane. The Fe atoms near the interface approach the C atoms, and the lines of the Fe atoms are bent, while the Nb atoms near the center of the interface move toward the [001] direction to maintain their distance from the Fe atoms. These features are consistent with the fact that the interface where the C atom exists on top of the Fe atom is preferable to that where the Nb atom exists on top of the Fe atom, as shown in Fig. 1. The lines through the Fe atoms, except for the two lines located near the center of the horizontal axis, are connected to C atoms at the interface. There is a region where only one C atom exists for the two lines through the Fe atoms near the center of the horizontal axis. In Fig. 2, this yellow region is a dislocation core.

The MDs were then attempted (performed) to estimate the amount of strain energy around the precipitate. The calculation cell was divided into two regions—the precipitate and matrix regions—although both regions were treated using the embedded-atom method (EAM) potential of Fe. The atomic positions were fixed so as to have the same lattice parameter as NbC in the hypothetical precipitate region. The strain energy was estimated by comparing the potential energies of the unit cells containing distorted or undistorted precipitate regions. Fig 3 shows the sum of the interface and strain energies plotted as functions of the length of the side of the precipitate for both the coherent and semicoherent precipitates and indicates that the growth of the precipitate leads to a transition from the coherent to the semicoherent state at 18- and 16-Å-long sides for precipitates that are 5.36 and 8.94 Å thick, respectively.

In summary, the interface and the strain energies of the interface between bcc iron and NbC were calculated using the $O(N)$ method of calculating electronic structures from first principles and using classical MD simulation. The lengths of the sides of the broad plane of the plate-like rectangular parallelepiped-shaped precipitates were also estimated at the transition from the coherent to the semicoherent interface.

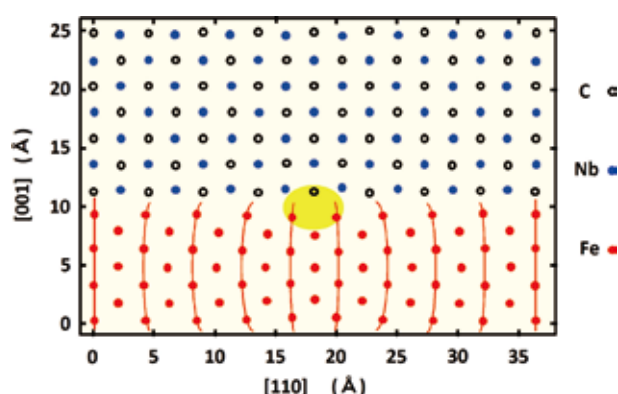


Fig. 2 Atomic configuration of semicoherent interface in (110) plane. For easy visualization, Fe atoms are connected by lines along [001] direction. Yellow region corresponds to dislocation core.

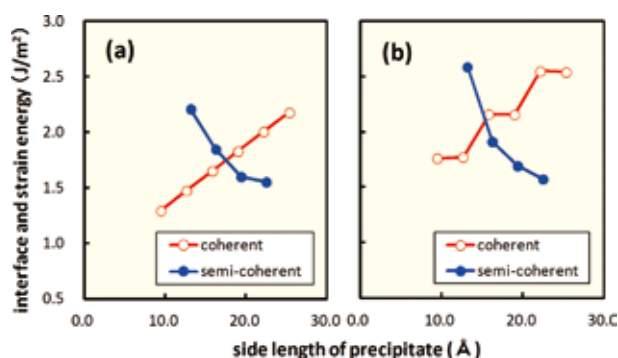


Fig. 3 Sum of interface and strain energies plotted as functions of the side length of the precipitate for coherent and semicoherent precipitates. Precipitates are (a) 5.36 and (b) 8.94 Å thick.

References

- [1] H. Sawada, S. Taniguchi, K. Kawakami, and T. Ozaki, Modelling Simul. Mater. Sci. Eng. **21**, 045012 (2013).
- [2] T. Ozaki, Phys. Rev. B **74**, 245101 (2006).